Control-Oriented Model of a Dual Equal Variable Cam Timing Spark Ignition Engine

A. G. Stefanopoulou*, J. A. Cook*, J. W. Grizzle†, J. S. Freudenberg†

October 31, 1997

Abstract

A control-oriented engine model is developed to represent a spark ignited engine equipped with a variable cam timing mechanism over a wide range of operating conditions. Based upon laboratory measurements a continuous, nonlinear, low-frequency phenomenological engine model is developed. With respect to a fixed-cam timing engine, the VCT mechanism alters the mass air flow into the cylinders, the torque response, and the emissions of the engine. The developed model reflects all of these modifications and includes a representation of the breathing process, torque and emission generation, and sensor/actuator dynamics. The model has been validated with engine-dynamometer experimental data and can be used in powertrain controller design and development.

Keywords: engine modeling, emission, camshaft timing, automotive powertrain, multivariable control

1 Introduction.

Modern automobile engines must satisfy the challenging and often conflicting goals of minimizing exhaust emissions, providing increased fuel economy and satisfying driver performance requirements over a wide range of operating conditions. An innovative mechanical design approach to achieving these goals has been the development of variable cam timing (VCT) engines.

Variable cam timing (VCT) is a promising feature for automotive engines because it allows optimization of the cam timing over a wide range of engine operating conditions. The majority of conventional engines operate at a fixed cam timing that provides a tradeoff among idle stability, fuel economy, and maximum torque performance. There are also successful examples of two-position cam timing engines that alleviate the above tradeoff by allowing operation in two cam timing settings. Investigation of variable cam timing schemes shows potential benefits in fuel economy (Elrod and Nelson, 1986; Ma, 1988; Gray, 1988), reduced feedgas emissions (Meacham, 1970; Stein et all., 1995), and improvement of full load performance (Lenz et al., 1988). There are four variable cam timing strategies possible for double overhead camshaft engines (DOHC): (i) phasing only the intake cam (intake only), (ii) phasing only the exhaust cam (exhaust only), (iii) phasing the exhaust

* Ford Motor Company, Scientific Research Laboratory, PO Box 2053, Mail Drop 2036 SRL, Dearborn, MI 48121, Fax: (313) 248-3611, Phone: (313) 322-1977

† Control Systems Laboratory, Department of Electrical Engineering and Computer Science, University of Michigan, Ann Arbor, MI 48109-2122; work supported in part by the National Science Foundation under contract NSF ECS-92-13551; matching funds to this grant were provided by FORD MO. CO.

and the intake cam equally (dual equal), and (iv) phasing the exhaust and the intake cam independently (dual independent). Static analysis and comparison of the effects of the four strategies at part load are given in (Leone et al., 1996).

In all four VCT schemes, cam timing can increase internal residual gas and consequently alter the intake, combustion and exhaust processes. Internal residual gas reduces the combustion temperature, thereby suppressing NO_x formation. The exhaust gas that is drawn back into the cylinder and reburned is rich in unburned HC. As a result, variable cam timing is used to reduce the base HC and NO_x feedgas emission levels of the engine with respect to a conventional powerplant with fixed cam phasing. The VCT mechanism can replace the external exhaust gas recirculation (EGR) system commonly used for NO_x reduction by achieving lower tailpipe emissions at equivalent catalytic converter efficiencies.

Variable cam timing schemes have a profound effect on the engine breathing process. Most VCT schemes require operation in higher manifold pressure. This results in reduction in pumping losses and therefore increased fuel economy. The dilution of the in-cylinder mixture, however, alters the engine torque response and leads to a tradeoff between low emissions and good drivability. The impact of the dual equal VCT scheme in torque response is more significant than the impact of the intake only and exhaust only VCT schemes and requires evaluation of the overall system performance. Dynamic cam timing scheduling requires the understanding of the interaction of the VCT subsystem with the other engine subsystems that affect emissions and engine performance.

To this end, we develop a nonlinear, low-frequency, phenomenological model of an experimental SI engine equipped with a dual-equal variable cam timing mechanism. A schematic representation of the dual-equal scheme is shown in Figure 1. The developed model con-

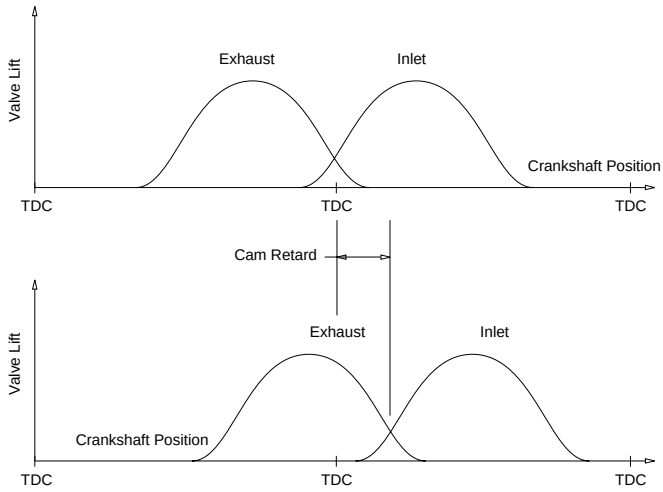

Figure 1: Schematic representation of the dual-equal VCT scheme. By retarding the cam phasing, the exhaust and intake valve overlap occurs later during the intake event. This causes the induction and reburn of the last part of the exhaust gases which is rich in unburned HC. The resulting dilution also lowers the combustion temperature and suppresses feedgas NO_x emissions. The amount of emission reduction will vary with engine speed and load.

sists of a representation of the breathing process, the torque generation and the feedgas NO_x and HC exhaust emissions. It also includes actuator/sensor dynamics and the important process and computational delays. It accurately represents the dynamic nonlinear and multivariable behavior of the VCT engine. The derived model can be used in powertrain control development with primary emphasis in reducing emissions while satisfying

drivability requirements at part load and medium engine speed. Furthermore, it can be used in assessing the feasibility and the achievable performance of the VCT engine when compared to a conventional external-EGR engine. Projections of vehicle performance can be based on simulation of the derived model during Federal Test Procedure (FTP) cycles. The dual-equal variable cam timing subsystem represents one of the various functional modes available with a camless engine (Schechter and Levin, 1996). The model structure presented here can be extended to a SI engine with a camless valvetrain.

This paper is organized as follows. After a brief definition of the variables used in the model description in Section 2, and a discussion of the experimental set-up in Section 3, the dual-equal VCT engine model is presented in Section 4. The assumptions made to modify the conventional engine model (Crossley and Cook, 1991) to incorporate the effects of dual-equal cam timing are tested in Section 5.1. In Section 5.2, the identified model is validated against actual engine-dynamometer data. Issues regarding the region of validity of the identified model are discussed in Section 5.3. In Section 6, the VCT engine model characteristics are analyzed from a control development perspective. Finally, in Section 7 we give some concluding remarks and discuss directions for future work.

2 Nomenclature

A/F	air-to-fuel ratio
c	coefficients on physical equations (with various subscripts)
	command when used in subscripts
CAM	camshaft timing (degrees)
F_c	fuel command (grams per intake event)
K, or k	static gains derived after linearization
$\dot{m}$	mass air flow ($\frac{g}{sec}$)
	$\dot{m}_\theta$: mass air flow through the throttle body
	$\dot{m}_{cyl}$: mass air flow to the cylinder
m	mass (g)
	m_a : mass air charge ($\frac{g}{event}$)
MAF	mass air flow measured at the hot wire anemometer
N	engine speed (RPM)
P	pressure (bar)
	P_m : manifold pressure (bar)
	P_o : ambient pressure (bar)
R	specific gas constant ($\frac{J}{kg \cdot K}$)
T	temperature (K)
T_q	engine brake torque (Nm)
V_m	manifold volume (m^3)
ΔT	fundamental sampling time interval (sec)
θ	throttle angle (degrees)
τ	time constant in lowpass filters (sec)

3 Experimental Set-up

The VCT experimental engine was mounted in a 300HP DC dynamometer. Measurements were collected using a UNIX-based data acquisition system. Air-to-fuel ratio was measured using an NTK Universal Exhaust Gas Oxygen (UEGO) sensor. The actual cam phasing

position was measured in the experimental set-up using an optical encoder with 1 degree resolution. Feedgas CO_2, CO, HC, and NO_x emission measurements were collected using a Horiba analyzer. The emission measurements were the averaged value of the contents of the emitted exhaust gas during 60 sec of steady-state engine operation. A hot wire anemometer was used to measure the mass air flow rate into the manifold. The sensor was located upstream of the throttle body. Measurements of brake torque on the dynamometer were used for steady-state engine mapping. In-cylinder pressure transducers (Kistler) were used to calculate indicated mean effective pressure (IMEP) and reconstruct the dynamic brake torque response during transient tests. The experimental engine was equipped with the necessary sensors for collecting inlet manifold pressure and various significant engine temperatures.

The dynamic tests consisted of small steps in throttle, cam timing, and fuel charge. During these dynamic tests, engine speed was kept constant (the dynamometer was set to speed mode). Feedforward load control was necessary to maintain constant engine speed during these dynamic tests because the dynamometer controller couldn't provide sufficiently fast closed loop engine speed control. For each step test, MBT spark timing was identified off-line and was controlled by using the test cell electronic management system. All experiments were performed with zero external exhaust gas recirculation.

To ensure accuracy and consistency of the dynamic throttle steps, a DC motor was used. With the DC motor, a throttle step of 90 degrees was achievable in 50 msec. The dynamic throttle tests were performed at a number of engine operating conditions, keeping cam timing constant, and using open-loop fuel and spark control to maintain engine operation at stoichiometry and to achieve MBT spark timing during step-test. Transient cam timing tests were performed to identify the engine dynamic behavior during changes in cam timing. During these transient tests, open loop spark and fuel control were employed while throttle angle and engine speed were kept constant.

4 Model Development.

The goal in controlling the VCT engine is to reduce tailpipe emissions, while maintaining driving behavior similar to a conventional engine. Tailpipe emissions depend on the catalytic converter efficiency and the amount of feedgas emission that the catalytic converter has to process. The catalytic converter efficiency is very sensitive to A/F deviations from the stoichiometric value. Therefore, we can correlate the catalytic converter efficiency with the A/F response. In the model developed we identify how throttle position, cam timing, and fuel charge affect torque, feedgas NO_x and HC, and A/F response. Emission levels are heavily studied and regulated in the engine-load range that corresponds to the Federal Test Procedure (FTP) cycle. For this reason, our modeling effort concentrates on the development of a control-oriented model of the experimental VCT engine in the region defined by the FTP cycle and is centered in the part-throttle medium-speed operating regime. Using this range of speed-load, we determine the set points of the independent variables of the engine and define the set of dynamometer experimental data for the model development.

The model derived in this paper represents spatially and event averaged quasi-steady time-varying phenomena. It fails, however, to describe high frequency phenomena due to acoustic and inertia dynamics, or the spatial variation of gas properties due to unsteady gas dynamics. It is a continuous, nonlinear, low-frequency, phenomenological representation of an eight cylinder experimental VCT engine, based on the engine model structure in

(Crossley and Cook, 1991; Powell and Cook, 1987; Moskwa and Hedrick, 1992; Cho and Hedrick, 1989; Dobner, 1980), with appropriate modifications for variable cam timing.

The dynamic elements of the engine model are described by physically based equations, whereas the pseudo-static elements are described by empirically based expressions as in (Crossley and Cook, 1991). The structure of the VCT engine model was identified by engine-dynamometer experiments; the VCT mechanism was found to alter the mass air flow into the cylinders, the internal EGR, the engine torque response, and exhaust emissions. The mass air flow through the throttle body, engine pumping rate, brake torque generation and feedgas NO_x and HC emissions generation are complex functions, depend on many engine parameters, and are difficult to model analytically, so they are included as nonlinear static empirical relations. Their parameters are determined from regressed dynamometer-engine steady-state data using the least squares approach. Physically based differential and difference equations are used to describe the dynamic elements of the engine, such as inlet manifold dynamics and the time delay elements in the signal paths. The identification of these parameters is based on the dynamic response of the experimental engine mounted in the dynamometer to small step inputs. Furthermore, the model includes actuator and sensor dynamics, and some important computational delays.

4.1 Manifold Filling Dynamics.

The intake manifold can be represented as a finite volume based on the "Filling and Emptying Methods" of plenum modeling described in (Heywood, 1988). The dynamic equations that characterize the manifold filling dynamics are based on the principles of conservation of mass, conservation of energy, and the ideal gas law given below :

$$\dot{m} = \sum_{i=1}^{I} \dot{m}_{in_i} - \sum_{j=1}^{J} \dot{m}_{out_j} \tag{1}$$

$$mc_v\dot{T}_m = \dot{Q}_m + \sum_{i=1}^{I}(c_{p_i}T_{in_i} - c_{v_i}T_m)\dot{m}_{in_i} - RT_m\sum_{j=1}^{J}\dot{m}_{out_j} \tag{2}$$

$$P_m = \varrho RT_m = \frac{m}{V_m}RT_m \ , \tag{3}$$

where c_p and c_v are the constant pressure and volume specific heat, m is the mass within the manifold at any time, Q is the heat flow into the manifold, R is the specific gas constant, and P_m, T_m, and V_m the manifold pressure, temperature and volume.

The equation of conservation of energy (Equation 2) is satisfied by assuming constant temperature and zero heat transfer to the walls. To use the state equation (Equation 3), the air into the intake manifold is assumed to be homogeneous. In addition to the above equations, the principle of conservation of momentum is also satisfied by assuming uniform pressure and temperature between the throttle body and the intake valves. Also we neglect the effects of backflow and leakage. This assumption might not be valid for all engine operating conditions. It is, however, a valid assumption for the speed-load region at which the engine model is identified. We assume zero exhaust gas into the manifold because exhaust gas is recirculating directly through the exhaust manifold and not through the inlet manifold. Therefore, we do not account for the effects due to the partial pressure of the exhaust gas in the inlet manifold.

Based on the previous equations and assumptions, the manifold filling dynamics can be described by the following first order differential equation that relates the rate of change of the manifold pressure (P_m) to the mass air flow rates into and out of the manifold ($\dot{m}_\theta$ and

$\dot{m}_{cyl}$, respectively)

$$\frac{d}{dt}P_m = k_m(\dot{m}_\theta - \dot{m}_{cyl}), \text{ where } k_m = \frac{R \cdot T_m}{V_m} \quad . \tag{4}$$

The value k_m can be derived by its physically based parameters $k_m = \frac{R \cdot T_m}{V_m}$, where $R = 287$ $\frac{J}{kg \cdot K}$ the specific gas constant, $T_m = 288$ K the nominal manifold temperature, and $V_m = 0.007$ m^3 the manifold volume, resulting in $k_m = 11808 \cdot 10^5$ $\frac{J}{kg \cdot m^3} = 0.118 \frac{bar}{g}$.

4.2 Flow through the Throttle Body

A quasi-steady model of flow through an orifice is used to derive the mass air flow through the throttle body into the manifold. The quasi-steady relation of the air flow through a valve opening is based on the assumptions of one-dimensional, steady, compressible flow of an ideal gas. The general equation describing the mass air flow across a valve opening was developed in (Novak, 1977):

$$\dot{m} = A_e P_u \left[\frac{\gamma}{RT_u}\right]^{0.5} \cdot \varphi, \text{ and } \varphi = \begin{cases} (\frac{2}{\gamma-1})^{\frac{1}{2}} \sqrt{(\frac{P_d}{P_u})^{\frac{2}{\gamma}} - (\frac{P_d}{P_u})^{\frac{\gamma+1}{\gamma}}} & \text{if } (\frac{P_d}{P_u}) > (\frac{2}{\gamma+1})^{\frac{\gamma}{\gamma-1}} \\ (\frac{2}{\gamma+1})^{\frac{\gamma+1}{2(\gamma-1)}} & \text{if } (\frac{P_d}{P_u}) \leq (\frac{2}{\gamma+1})^{\frac{\gamma}{\gamma-1}} \end{cases}$$

where A_e is the effective flow area, P_u and T_u are the upstream pressure and temperature, P_d is the downstream pressure, and $\gamma = \frac{c_p}{c_v}$ is the ratio of specific heats.

Based on the above relation we can derive the mass air flow rate into the manifold ($\dot{m}_\theta$) through the primary throttle body as a function of the throttle angle (θ), the upstream pressure (P_o), which we assume to be close to the atmospheric, i.e., $P_o = 1$ bar, and the downstream pressure, which is the manifold pressure (P_m). The simplified function describing $\dot{m}_\theta$ is given in (Crossley and Cook, 1991):

$$\dot{m}_\theta = g_1(P_m) \cdot g_2(\theta), \quad \text{where } g_1(P_m) = \begin{cases} 1 & \text{if } \frac{P_m}{P_o} \leq \frac{1}{2} \\ 2\sqrt{\frac{P_m}{P_o} - (\frac{P_m}{P_o})^2} & \text{if } \frac{P_m}{P_o} > \frac{1}{2} \end{cases} \tag{5}$$

and $g_2(\theta)$ is a third order polynomial in throttle angle. The regressed equation for $g_2(\theta)$ can be found in the Appendix. Figure 2 shows the mass air flow through the throttle body ($\dot{m}_\theta$) for different values of θ.

4.3 Engine Pumping Rate

The pulsating mass air flow out of the manifold and into the cylinders is a complicated function of engine characteristics, the conditions in the intake and exhaust manifold, and the gas inertia. It can be represented, however, by an empirical relationship assuming quasi-steady operating conditions, and averaging the mass air flow into the cylinders over an engine event. The empirical relationship can be developed by treating the engine as a pump and assuming constant intake temperature and exhaust gas pressure. The engine pumping mass air flow rate ($\dot{m}_{cyl}$) for a conventional engine is a function of manifold pressure (P_m), and engine speed (N). Retarded cam timing increases the exhaust gas recirculation and therefore decreases the fresh mass air flow into the cylinders. The regressed mass air flow rate is a polynomial in cam phasing (CAM), manifold pressure (P_m), and engine speed (N). The resulting polynomial is of degree three, and a third order polynomial in each individual variable:

$$\dot{m}_{cyl} = F(CAM, P_m, N) \quad . \tag{6}$$

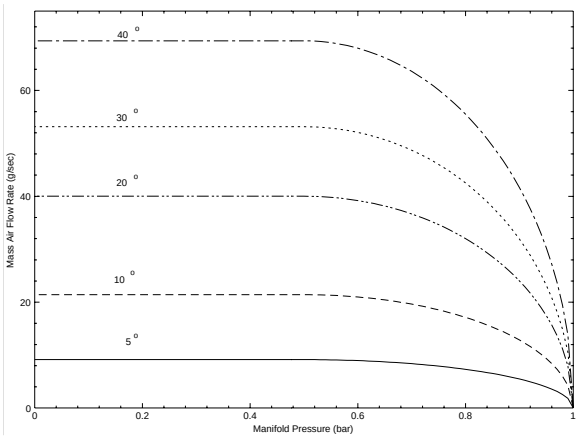

Figure 2: Mass air flow rate through the throttle body as a function of manifold pressure for different throttle angles.

The identified polynomial can be found in the Appendix. Figure 3 shows the variation of mass air flow rate with manifold pressure (P_m) for different values of cam phasing (CAM) at constant engine speed (1000 RPM).

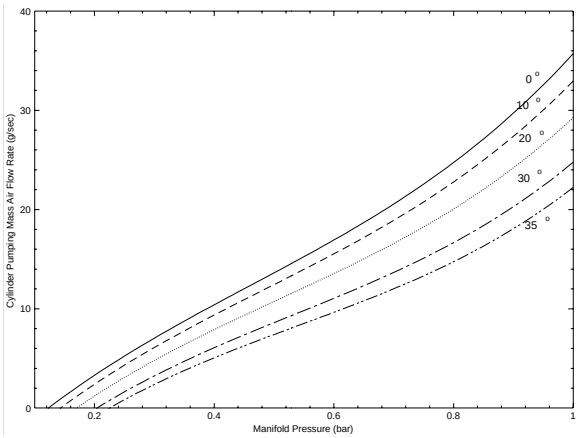

Figure 3: Engine pumping mass air flow rate as a function of manifold pressure for five different cam timing values at 1000 RPM.

4.4 Torque Generation.

The generation of engine torque is a complex process that depends on geometric cylinder and valve features, thermodynamic properties of the unburned and burned gases, the mass and energy equation and the combustion process. The brake torque model derived here is an empirical static relationship of measurable parameters and assumes that fuel, air, and the residual gas are uniformly mixed, and quasi-steady engine operation with the individual cylinder torque generation averaged over one engine event.

During the steady-state engine mapping, spark timing is scheduled at minimum spark advance to achieve best torque (MBT). Therefore the identified torque response corresponds to MBT spark timing, and consequently spark is not an independent variable for the developed VCT engine model. This approach is justified since the effects of spark timing on torque are almost instantaneous when compared to the effects of air charge, air-to-fuel ratio,

and exhaust gas recirculation.

Based on the experimental data of the steady-state torque response, we have concluded that cam timing affects brake torque through its effects on the fresh air charge into the cylinders. The basis functions used in regressing brake torque are similar to the ones generally used in modeling brake torque of conventional engines (Crossley and Cook, 1991). Therefore, engine torque (T_q) can be mapped as a function of the air charge (m_{cyl}), the air fuel ratio (A/F), and the engine speed (N). The modeled torque equation is a polynomial of degree three, and a third order polynomial in each individual variable :

$$T_q = F(m_{cyl}, A/F, N) \quad . \tag{7}$$

The equation for brake torque is contained in the Appendix. The variation of torque with A/F for different values of cylinder air charge (grams per intake event) at constant engine speed (1500 RPM) is shown in Fig. 4.

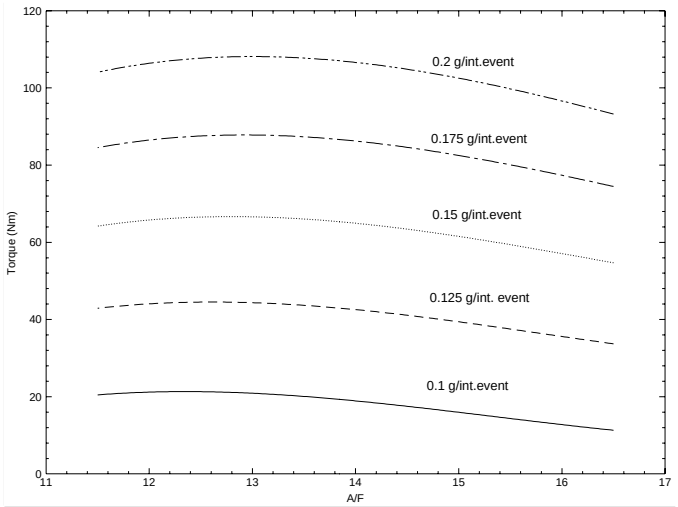

Figure 4: Engine torque as function of A/F for different values of air charge at constant engine speed (1500 RPM).

To obtain a dynamic prediction of torque we superimpose on the multivariate static relationship the induction to power stroke delay. Other dynamic phenomena associated to the combustion process have time constants that are too small to be considered in a real-time control strategy.

4.5 Feedgas NO_x and HC emissions.

By NO_x emissions, we mean the group of nitric oxides NO and nitric dioxides NO_2 produced inside the engine cylinder. In SI engines, experiments and chemical equilibrium considerations indicate that at typical flame temperatures NO_2/NO ratio are negligible. The principle source of NO is the oxidation of atmospheric (molecular) nitrogen since gasoline contains negligible amounts of nitrogen. Nitric oxide forms in high-temperature burned gases. The higher the burned gas temperature the higher the rate of NO formation. Residual gas reduces the combustion temperature, and consequently reduces the NO formation. The most important engine variables affecting NO_x are the burned gas fraction of the unburned mixture, the A/F and the spark timing. For simplicity, the spark timing is scheduled at MBT. Regression of data from the dynamometer and the emission analyzer

result in an empirical relationship for the feedgas NO_x emissions. The quasi-static NO_x can be described by a polynomial in engine speed (N), cam phasing (CAM), air fuel ratio (A/F), and manifold pressure (P_m). The four variable regression applied in the NO_x emission data results in an eighth degree polynomial. The modeled NO_x equation is a second, first, third and second order polynomial in engine speed (N), cam phasing (CAM), air fuel ratio (A/F), and manifold pressure (P_m), respectively :

$$NO_x = F(N, CAM, A/F, P_m) \quad . \tag{8}$$

The exact coefficients from the regression analysis can be found in the Appendix. Figure 5 shows the NO_x dependency on A/F and CAM phasing. Studies about the prediction of dynamic NO_x emissions based on the static engine mapping (Throop et al., 1985) show that the dynamic NO_x is also a function of the dynamic cylinder wall temperature. This dependency is not included in this study and might result in the predicted level of NO_x emission being higher than the actual level during an acceleration-deceleration maneuver.

Feedgas HC emissions are the result of incomplete combustion of the hydrocarbons in the fuel. HC formation is based on four complex mechanisms even under the assumption that fuel, air, and residual gas form a uniform mixture. The mechanism of flame quenching at the combustion chamber walls results in a layer of unburned HC attaching to the cylinder wall that is consequently scraped off by the piston and expelled from the cylinder during the last phase of the exhaust stroke (Heywood, 1988). By retarding the cam phasing, we keep this last part of the exhaust gases in the cylinder and reburn it.

The feedgas HC emissions can be modeled by an empirical function of independent engine variables. The modeled HC emission equation is a polynomial in the engine speed (N), cam phasing (CAM), air fuel ratio (A/F), and inverse manifold pressure ($\frac{1}{P_m}$). The derived equation describing HC emissions is given by :

$$HC = F(N, A/F, \frac{1}{P_m}, CAM) \quad . \tag{9}$$

Figure 6 shows the variation of HC emissions with A/F and cam phasing at constant manifold pressure ($P_m = 0.4$ bar), and engine speed ($N = 2000$ RPM).

The exact function that represents the HC emissions can be found in the Appendix. In (Hamburg and Throop, 1984) it is shown that dynamic feedgas HC emissions can be accurately predicted by the regression analysis of static measurements.

4.6 Process Delays.

The fundamental sampling rate for an n cylinder engine at engine speed N (revolutions per minute) is $\frac{1}{\Delta T} = \frac{N \cdot n}{120}$, where ΔT (seconds) is the fundamental sampling time interval. The discrete nature of the engine causes delays in the signal paths. For the engine studied, a delay of $4\Delta T$ seconds is assumed between the induction of the air and fuel mixture into the cylinders, and the corresponding torque response; this corresponds to the physical delay in induction-to-power. The NO_x and HC emissions are steady state measurements (average values) and cannot be measured dynamically. Their identified static nonlinear maps, however, will be included in the VCT model in the same dynamic manner as the torque generation function.

A delay of $9\Delta T$ seconds is also identified between the mass charge formation and the time when its corresponding exhaust gas reaches the EGO sensor. This delay corresponds to a $4\Delta T$ seconds delay in the induction-to-power stroke process, a $4\Delta T$ seconds delay in the power-to-exhaust stroke process, and a ΔT seconds delay in the transport process

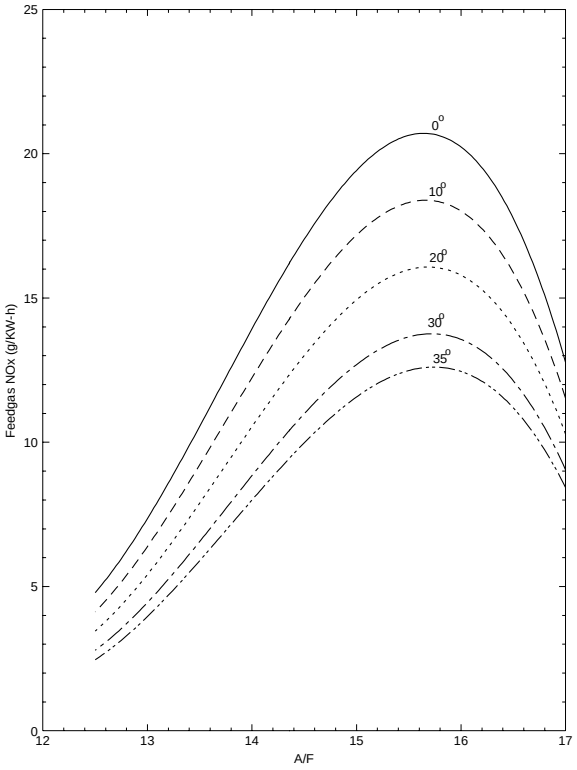

Figure 5: Feedgas NO_x emission plotted versus A/F for different CAM timing values at constant manifold pressure ($P_m = 0.4$ bar), and engine speed ($N = 2000$ RPM).

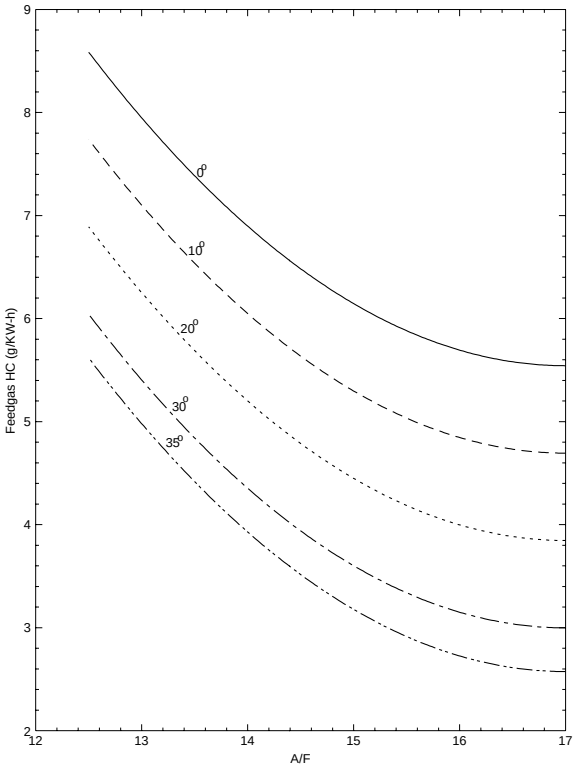

Figure 6: Feedgas HC emission versus A/F for different CAM timings at constant manifold pressure ($P_m = 0.4$ bar), and engine speed ($N = 2000$ RPM).

in the exhaust manifold. To achieve good combustion properties, the fuel is injected on closed intake valves, i.e., during the exhaust stroke prior to the intake event. Including the computational delay involved in the fuel pulse width calculation, a total delay of $2\Delta T$ seconds is estimated between the commanded fuel pulse width and the formation of its corresponding charge.

4.7 Actuators and Sensors.

The dynamics of the VCT actuator were identified using parametric identification methods from the Matlab system identification toolbox and are described by the following transfer function :

$$\frac{CAM_{actual}}{CAM_{commanded}} = \frac{-0.706s + 705.8}{s^2 + 16.13s + 705.8} \quad . \tag{10}$$

For control purposes, this transfer function was approximated by :

$$\frac{CAM_{actual}}{CAM_{commanded}} = \frac{-0.013s + 26.959}{s + 26.959} \quad . \tag{11}$$

The dynamics of the EGO sensor are modeled as a first order lag followed by a preload (relay or switching-type) nonlinearity. The preload nonlinearity in the EGO sensor is viewed as a coarse form of quantization which can be adjusted in a later design phase. The time constant of the EGO sensor is typically 70 msec.

A hot wire anemometer is used to measure the mass air flow rate through the throttle body. A first order lag with time constant equal to 27 msec is used to describe the air meter dynamics. Finally, cam phasing measurements in a vehicle implementation were considered to be updated every event introducing a delay of ΔT seconds between the actual and the measured cam timing.

5 Validation

The test work here involves the comparison of the identified model response with actual engine data to small step inputs. The set of data used for the validation is different from the set of data used for the model development. The work here provides validation of the breathing and combustion process, and the sensor/actuator dynamics. Validation of the dynamic emission model was not possible with the available emission analyzers.

5.1 Breathing Process Structure.

In this section we verify the breathing model structure and check the validity of the assumptions employed in the previous chapters. Simple experiments of fast throttle and cam timing changes were used to validate the model structure before proceeding with the full scale parameter identification. When the structure is defined and validated, static and dynamic experiments can be specified to identify the parameter of the phenomenological model. The phenomenological model can be easily updated to represent different platforms by calibrating the numerical values of the model parameters.

Validation of the breathing process is a crucial step in the development of the VCT engine, because the breathing process affects the torque, fuel economy, and feedgas emission generation of an SI engine. The validation of the breathing process is based on our ability to determine the value of k_m in the ideal gas law (Equation 4) based on experimental data and the assumed model structure. The experimentally derived k_m is subsequently compared with the physically based k_m ($k_{m_{<phys>}} = \frac{RT_m}{V_m}$). During transient throttle and cam timing step tests engine speed is kept constant. The step changes in throttle and cam timing are selected to maintain sonic flow throughout the transient tests. Measurements of the actual throttle angle, actual cam timing, mass air flow upstream the throttle body, and manifold pressure were logged during the experiments. Voltage signals were used to eliminate any calculation delays and were then scaled based on their steady-state value. The nonlinear equations used to represent the breathing process for constant engine speed are :

$$\left.\begin{array}{ll} \frac{d}{dt}P_m(t) & = K_m(\dot{m}_\theta(t) - \dot{m}_{cyl}(t)) \\ \dot{m}_\theta(t) & = g_1(P_m(t)) \cdot g_2(\theta(t)) \overset{sonic}{\underset{flow}{=}} g_2(\theta(t)) \\ \dot{m}_{cyl}(t) & = F(CAM(t), P_m(t), N_o(t)) \end{array}\right\} \overset{linearization}{\Rightarrow} \begin{array}{ll} \frac{d}{dt}\Delta P_m & = k_m(\Delta\dot{m}_\theta - \Delta\dot{m}_{cyl}) \\ \Delta\dot{m}_\theta & = k_\theta \Delta\theta \\ \Delta\dot{m}_{cyl} & = -k_{p1}\Delta CAM + k_{p2}\Delta P_m \end{array} ,$$

where k_θ and k_{pi} (for i=1,2,3) are positive constants.

The transfer function between manifold pressure, mass air flow rate and cam timing is given by:

$$\left.\begin{array}{ll} \Delta\dot{m}_{cyl} & = -k_{p1}\Delta CAM + k_{p2}\Delta P_m \\ \frac{d}{dt}\Delta P_m & = k_m(\Delta\dot{m}_\theta - \Delta\dot{m}_{cyl}) \end{array}\right\} \Rightarrow \Delta P_m = \frac{k_m}{s + k_m k_{p2}}\Delta\dot{m}_\theta + \frac{k_m k_{p1}}{s + k_m k_{p2}}\Delta CAM \quad (12)$$

Letting $\tau_m = \frac{1}{k_m k_{p2}}$ the manifold pressure can then be expressed as

$$\Delta P_m = \frac{\frac{1}{k_{p2}}}{\tau_m s + 1}\Delta \dot{m}_\theta + \frac{\frac{k_{p1}}{k_{p2}}}{\tau_m s + 1}\Delta CAM \ . \tag{13}$$

The dynamics of the manifold absolute pressure (MAP), the mass air flow (MAF), and the cam position sensor can be expressed as :

$$\Delta MAP = \frac{1}{\tau_p s + 1}\Delta P_m, \quad \Delta MAF = \frac{1}{\tau_h s + 1}\Delta \dot{m}_\theta, \ \text{ and } \ \Delta CAM_m = e^{-\tau_c s}\Delta CAM \ , \tag{14}$$

We can neglect the above sensor dynamics because their time constants (τ_p, τ_h, τ_c) are significantly smaller that the manifold filling time constant (τ_m) . The resulting transfer function between the measured manifold pressure, the measured mass air flow rate and the cam measurement is given by :

$$\Delta MAP = \frac{\frac{1}{k_{p2}}}{\tau_m s + 1}\Delta MAF + \frac{\frac{k_{p1}}{k_{p2}}}{\tau_m s + 1}\Delta CAM_m \ . \tag{15}$$

Using Equation 15, the time constant τ_m can be experimentally determined during throttle and cam timing steps. The values of k_{p1} and k_{p2} can be derived from the linearization of a crude approximation of the engine pumping rate ($\dot{m}_{cyl}$) around the nominal operating point. Based on the experimentally evaluated τ_m and k_{pi}, k_m is calculated ($k_{m_{<exp>}} = \frac{1}{\tau_m k_{p2}}$) and compared with its theoretical value $k_{m_{<phys>}} = 0.118$ (see Section 4.1). After six experiments, the average value of the experimentally derived k_m is 0.12 with small standard deviation. Agreement of the experimentally derived k_m with the physically based k_m validates the model structure of the breathing process.

5.2 Engine Model.

During the validation experiments, engine speed and A/F are kept constant at 2000 RPM and the stoichiometric value, respectively. The spark timing is adjusted to MBT. Figure 7 shows the predicted and actual engine response during a step change in the throttle position. The upper plot in Figure 7 is the predicted and actual reading in the Hot Wire Anemometer (HWA) sensor during step changes in the throttle position. This plot shows a good agreement between (i) the modeled and actual air flow through the throttle body, and (ii) the modeled and the actual HWA sensor dynamics. The actual manifold pressure and the manifold pressure obtained from the developed simulation model are shown in the middle plot of Figure 7. The predicted engine torque response during the throttle step is compared with the reconstructed dynamic engine torque response at the lower plot of the same figure. The reconstructed dynamic torque response is calculated based on in-cylinder pressure measurements and a slow brake torque measurement.

Figure 8 shows the engine response during step changes in cam position. The upper plot in this Figure shows the simulated response of the identified VCT actuator model and the actual cam phasing. It can be seen that the identified model accurately represents the experimental VCT actuator dynamics. In the middle plot, the modeled breathing process dynamics is validated against experimental data by comparing the manifold pressure traces during the actual and the simulated dynamic cam tests. The lower plot in Figure 8 shows the predicted and actual torque response. Note that during this validation test the steady-state torque response is independent of the cam phasing. However the large torque drop during the cam phasing transition might be crucial to drivability requirements.

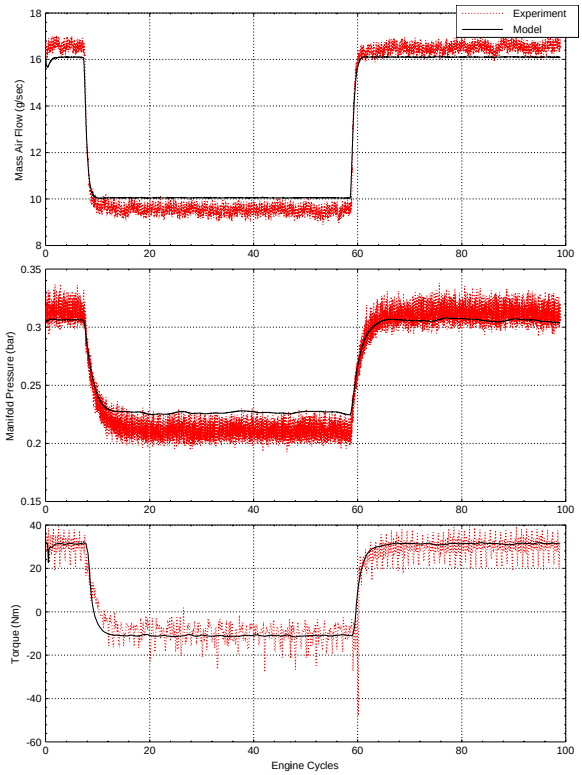

Figure 7: Model and actual dynamic response to throttle step command.

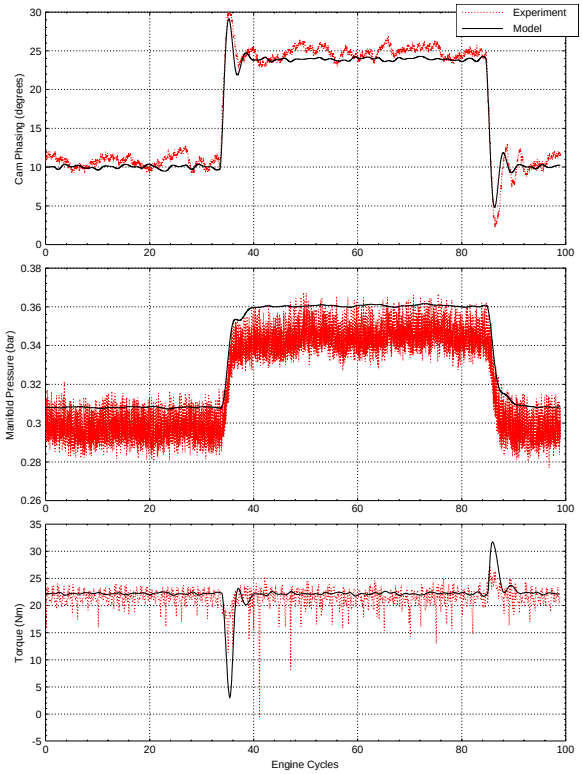

Figure 8: Model and actual dynamic response to cam phasing step command

5.3 Region of Validity.

The block diagram of the identified control-oriented VCT engine simulation model is shown in Fig. 9. The data collected for the identification of the VCT engine model lie between 750

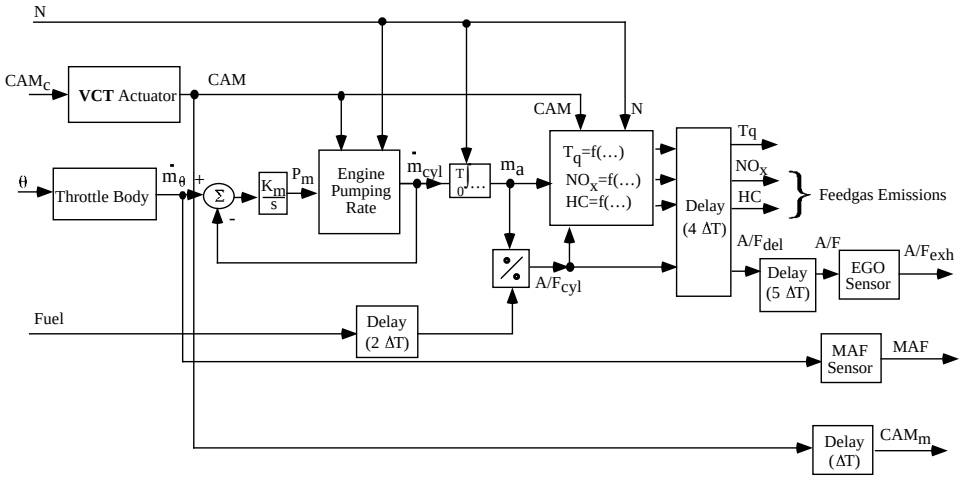

Figure 9: Block diagram of the identified control-oriented VCT engine model.

RPM and 2000 RPM, which covers most of the operating region in the current FTP cycle for this engine. The data collected represent engine operation for throttle positions less than 25 degrees; operation beyond this region requires extrapolation and should be used cautiously.

The derived model does not include fuel puddling dynamics, which is one of the important causes of A/F excursions during transient operation. The model of fuel puddling dynamics developed in (Aquino, 1981) can be added to the developed VCT engine model after studying the effects of cam timing on the time constant of the puddle generation (τ_f), and the fraction of evaporated fuel from the fuel film (X). This issue must be addressed if the model is used in A/F control design by evaluating the sensitivity of the designed control scheme to the uncertain dynamics.

The VCT engine model also does not include the rotational dynamics of the dynamometer, since engine speed is a slowly varying state with respect to breathing and A/F dynamics. For control development, however, engine speed must be a scheduling parameter. The experimental test-cell facility could not support the validation of the dynamic feedgas emission model which is derived based on static data and includes the intake-to-exhaust-stroke delay as the dominant dynamic process. This assumption should be tested in future modeling efforts. Also, the dynamic effects of cam timing on the pumping work during the intake stroke, which can alter the brake torque characteristics, are not pictured in the identified model.

Spark timing very rapidly affects engine torque response, emissions and efficiency. It is the fastest actuator among all the actuators available for engine control, but it is constrained by knock limitations. Knock depends on temperature, compression ratio and fuel properties. The identified VCT engine model assumes these parameters to be constant. Additional modeling effort should include the effects of cam timing on these parameters and their relation to spark timing control[1].

[1]Spark timing is a fast actuator but implementation of real-time embedded spark timing involves scheduling and processing delays that have to be included in a control oriented model.

6 Engine Characteristics from a Control Perspective.

The main objective of variable cam timing is to reduce feedgas emissions during part throttle operating conditions. Based on static engine mapping, we can optimize the cam timing to minimize feedgas emissions with the constraint of smooth static torque response. Rapid throttle movements are now accompanied by changes in cam phasing in order to minimize feedgas emissions. These changes affect the cylinder air charge and can cause (i) large A/F excursions and (ii) torque hesitation. Large A/F excursions reduce the catalytic converter efficiency and can nullify the VCT engine's main purpose of reducing engine emissions. Furthermore, drivability requirements might impose a severe limitation in cam movements. Restricting cam phasing might sacrifice the potential benefits of the VCT engine. Thus, it is essential to completely characterize and consider the effects of cam timing in the engine torque response and A/F control. In this section we are going to investigate these issues by analyzing the unique interactions of the cam timing with the engine torque and A/F response.

Cam timing alters engine torque response primarily by increasing the internal exhaust gas residuals. The temperature of the in-cylinder mixture increases. A rise in air charge temperature causes a decrease in air density. This requires operation at higher manifold pressure to achieve the same level of torque response. Since manifold pressure cannot change instantaneously, fast cam timing changes can cause unacceptable transient torque response. In addition, cam retard reduces the steady-state air flow into the cylinders when the air flow through the throttle body is subsonic. It does not affect, however, the steady-state value of air flow into the cylinders when the air flow through the throttle body is sonic.

To illustrate this phenomenon we write again the nonlinear equations that describe the breathing process during sonic flow in the throttle body:

$$\begin{aligned} \dot{m}_\theta &= g_1(P_m(t))g_2(\theta) \\ \dot{m}_{cyl} &= F(CAM, P_m, N) \\ \frac{d}{dt}P_m &= K_m(\dot{m}_\theta - \dot{m}_{cyl}) \end{aligned} \tag{16}$$

In quasi-steady engine operation, mass air flow and manifold pressure vary periodically with time as each cylinder draws air from the intake manifold, causing a pulsation with frequency equal to the fundamental engine frequency (see Sec. 4.6). The developed model predicts the averaged values of manifold pressure and mass air flow rate. The equilibrium of the breathing process occurs when $\dot{m}_\theta = \dot{m}_{cyl}$. Figure 10 shows different operating conditions and the corresponding equilibrium points for several throttle positions, engine speeds and cam timings. The steady-state manifold pressure and mass air flow into the cylinders is obtained at the intersection of the engine pumping rate curves ($\dot{m}_\theta$) with the mass air flow through the throttle curves ($\dot{m}_{cyl}$). In Figure 10, the intersection of the engine pumping rate curves ($\dot{m}_{cyl}$) at 2000 RPM for various values of cam timing with the mass air flow curves ($\dot{m}_\theta$) for throttle angle 9.0 degrees results in constant steady-state flow into the cylinders. Manifold pressure, however, varies at each intersection. Cam timing, therefore, alters the manifold pressure but does not affect the air flow into the inlet manifold during sonic conditions in the throttle body. During these conditions, a manifold pressure rise compensates in steady-state for the decreased air charge density caused by retarding the cam. One can observe the nonlinear behavior of the breathing process dynamics by comparing this result with the intersections of the engine pumping rate curves at 750 RPM with the air flow into the manifold that corresponds to the same throttle angle. The latter intersections occur during subsonic flow conditions and result in different values for the

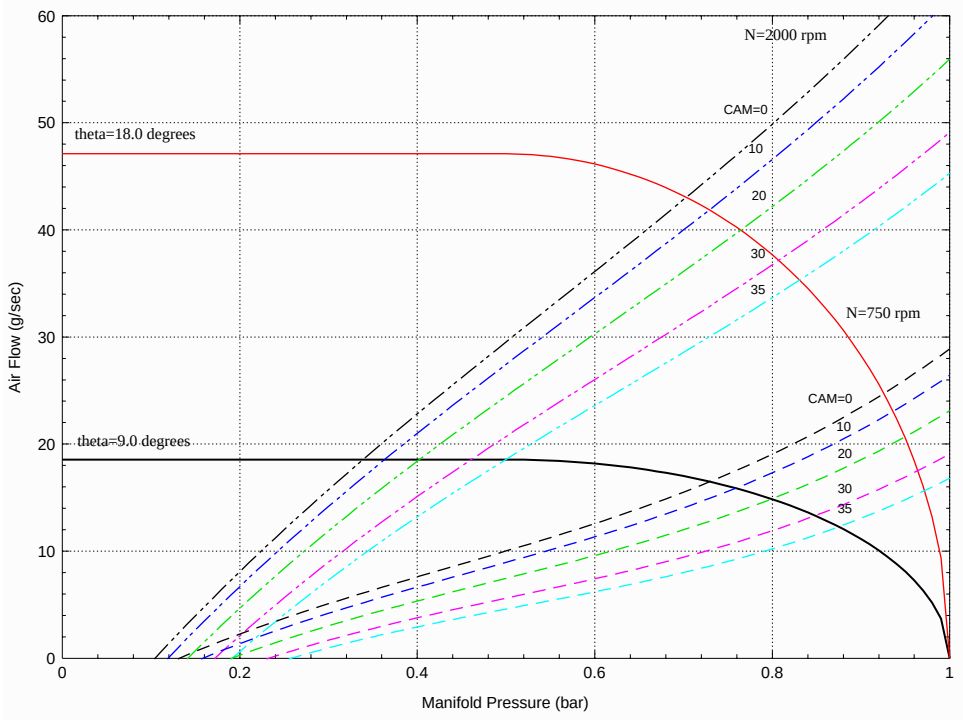

Figure 10: Mass air flow rate into ($\dot{m}_\theta$) and out ($\dot{m}_{cyl}$) of the manifold as a function of manifold pressure for two different engine speeds and five cam timing values.

manifold pressure and the air flow into the cylinders.

Figure 11 shows the steady-state torque response at 750 and 2000 RPM engine speed. Note that cam timing does not affect engine torque response for small throttle angles because of sonic flow conditions at the throttle body. At 750 RPM engine speed, however, subsonic flow occurs much earlier and torque response is very sensitive to cam timing even during very small throttle angles. Torque variation due to cam timing is important during low engine speeds because the driver is especially perceptive to torque changes there.

Linearization of the breathing dynamics (Equation 16 at constant engine speed) will elucidate further the dynamical characteristics at the two distinct operating points—sonic flow versus subsonic flow :

$$\begin{aligned} \Delta\dot{m}_\theta &= k_{\theta 1}\Delta\theta - k_{\theta 2}\Delta P_m \\ \Delta\dot{m}_{cyl} &= -k_{p1}\Delta CAM + k_{p2}\Delta P_m \\ \frac{d}{dt}\Delta P_m &= k_m(\Delta\dot{m}_\theta - \Delta\dot{m}_{cyl}) \ . \end{aligned} \tag{17}$$

The transfer function between CAM timing, throttle position, and mass air flow into the cylinders is given by:

$$\Delta\dot{m}_{cyl}(s) = \frac{k_m k_{\theta 1} k_{p2}}{s + k_m(k_{\theta 2} + k_{p2})}\Delta\theta(s) - \frac{k_m k_{p1} k_{\theta 2} + k_{p1} s}{s + k_m(k_{\theta 2} + k_{p2})}\Delta CAM(s) \ . \tag{18}$$

During sonic flow, air flow rate through the throttle body depends only on the throttle angle ($k_{\theta 2} = 0$) and $\Delta\dot{m}_\theta = k_{\theta 1}\Delta\theta$. Air flow rate into the cylinder for constant throttle angle is given by :

$$\Delta\dot{m}_{cyl}(s) = \frac{-k_{p1} s}{s + k_m k_{p2}}\Delta CAM(s) \ , \tag{19}$$

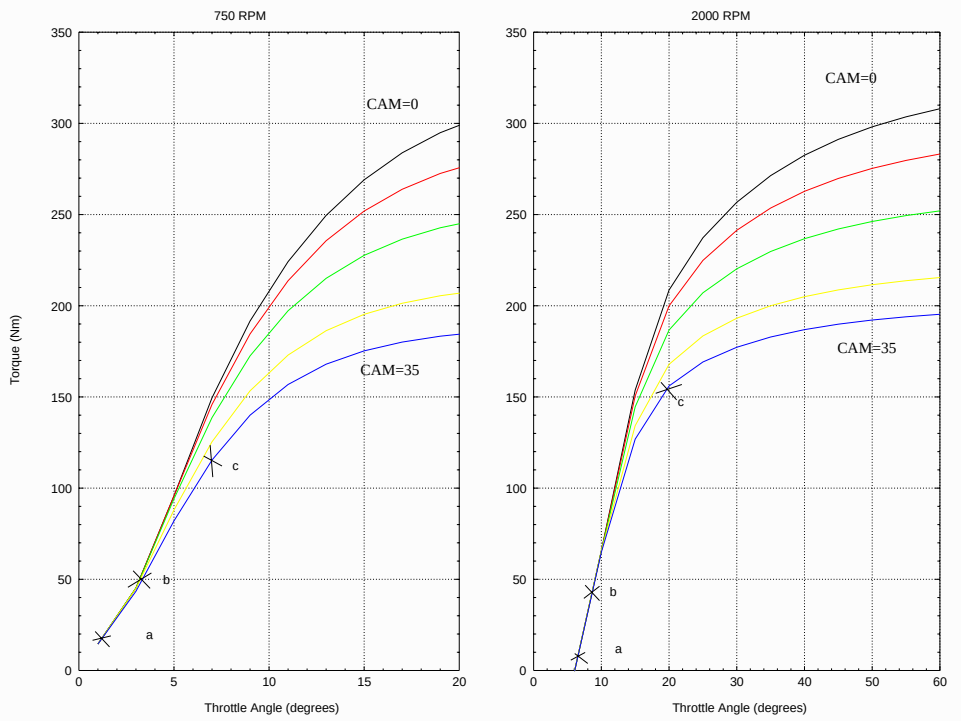

Figure 11: Steady-state torque response as a function of throttle angle for different cam timings at different engine speeds.

and the resulting engine torque response for constant A/F and engine speed (N) is given by:

$$\Delta T_q(s) = \frac{-k_T k_{p1} s}{s + k_m k_{p2}} \Delta CAM(s) \ , \tag{20}$$

where $k_T = \frac{\partial T_q}{\partial \dot{m}_{cyl}}$. The DC gain of the above transfer function is clearly zero. There is, however, a considerable coupling in higher frequencies between cam timing and torque response. This coupling can be seen in Figure 12 through the Bode gain plots of the transfer function between throttle and cam timing, and the engine outputs—torque and A/F. Figure 12 represents the linearized engine input-output relationship for three nominal throttle and cam timing operating points. These points are shown in Fig. 11 and represent a possible throttle and cam timing operating trajectory: point a, 8 degrees throttle and 0 degrees cam phasing; point b, 9 degrees throttle and 25 degrees cam phasing; point c, 20 degrees throttle and 35 degrees cam phasing. Changes in throttle position strongly influence torque response, and by comparing term p_{11} with term p_{12}, we can see a similar interaction between cam timing and torque. More precisely, the effect of cam timing on torque is 16 to 36 dB smaller than the effect of throttle on torque at frequencies near 11 rad/sec. Strong dependency between cam timing and A/F occurs at 15 rad/sec. This effect is 20 dB less than the effect of throttle on A/F. The latter is one of the primary causes of transient A/F excursions in conventional engines. Therefore, rapid changes in cam timing might affect the catalytic converter efficiency. The same characteristics can also be observed at 750 RPM. The peak, however, of the interaction between CAM timing and the engine outputs occurs at a lower frequency, 9 rad/sec. The interactions of cam timing with torque response and A/F indicate the need of a multivariable cam timing control design. A fairly extensive control analysis and design is carried out in (Stefanopoulou, 1996).

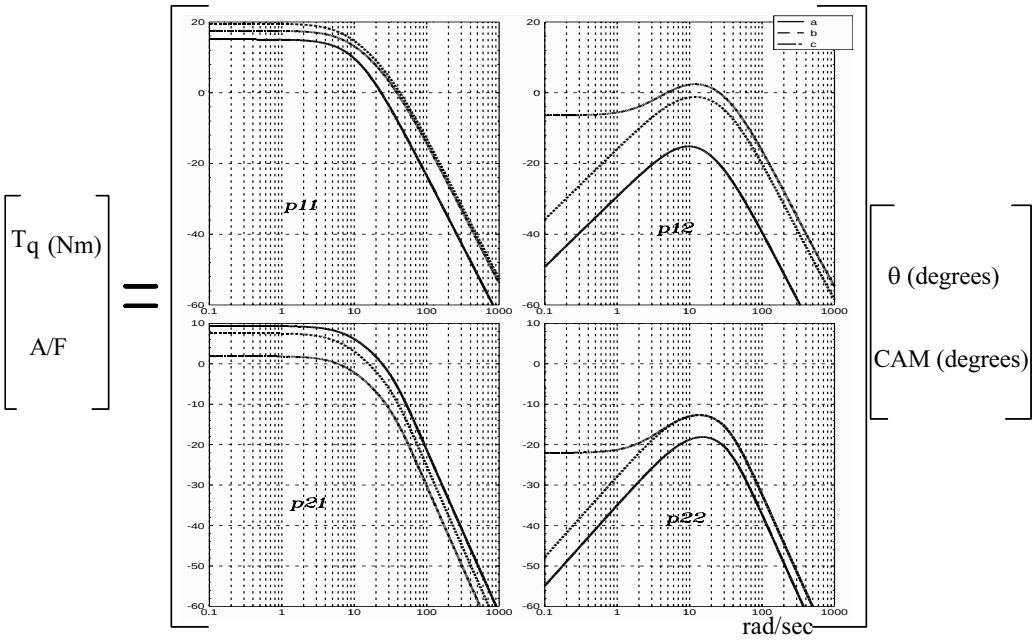

Figure 12: Bode gain plots of the open loop plant using engineering units. Inputs are throttle angle and cam timing, and outputs are torque and A/F. The three lines represent different operating conditions at constant engine speed (2000 RPM).

7 Conclusions.

A phenomenological model of an SI engine equipped with a dual-equal variable cam timing mechanism has been presented in this paper. The model includes the nonlinear representation of the breathing process, torque and emission generation, and sensor/actuator dynamics. The engine characteristics have been validated using engine-dynamometer experimental data. The developed model can be used for the analysis and control of the cam timing to reduce feedgas emissions during part throttle and medium speed operating conditions. Initial investigation of the VCT engine characteristics shows significant interactions between the following three engine performance indices: torque response, feedgas emissions, and air-fuel ratio. The variable cam timing engine is shown to be a multivariable system. The developed model is essential in assessing the performance tradeoffs between engine performance indices (drivability, emissions) in the development of a powertrain controller.

The dual-equal variable cam timing engine reflects a small subset of the optimum valve timing solutions that a camless engine can provide. Nevertheless, the dynamic interactions and control issues that arise in the dual-equal VCT engine are almost certain to appear in the highly interactive camless engine. The work in this paper is the first systematic approach towards studying and developing one of the various functionalities of a camless engine from a control perspective.

8 Acknowledgments

The authors thank M. Haghgooie, P. S. Szpak and M. Seaman for their support in assembling the experimental facility and collecting the data used in this work.

References

Aquino C. F., 1981, "Transient A/F Control Characteristics of the 5 Liter Central Injection Engine," SAE Paper No. 810494.

Cho D. and Hedrick J. K., 1989, "Automotive Powertrain Modeling for Control", ASME Journal of Dynamic Systems, Measurement, and Control, Vol. 111, pp. 568-576.

Crossley P. R. and Cook J. A., 1991, "Nonlinear Model for Drivetrain System Development," IEE Conference 'Control 91', Edinburgh, U.K., March 1991, IEE Conference Publication 332 Vol. 2, pp. 921-925.

Dobner D. J., 1980, "A Mathematical Engine Model for Development of Dynamic Engine Control", SAE Paper No. 800054.

Elrod A. C. and Nelson M. T., 1986, "Development of a Variable Valve Timing Engine to Eliminate the Pumping Losses Associated with Throttled Operation," SAE Paper No. 860537.

Gray C., 1988, "A Review of Variable Engine Valve Timing," SAE Paper No. 880386.

Hamburg D. R. and Throop M. J., 1984, "A Comparison Between Predicted and Measured Feedgas Emissions for Dynamic Engine Operation", SAE Paper No. 841256.

Heywood J. B., 1988, *Internal Combustion Engine Fundamentals,* McGraw-Hill.

Lenz H. P., Wichart K., and Gruden D., 1988, "Variable Valve Timing- A Possibility to Control Engine Load without Throttle," SAE Paper No. 880388.

Leone T. G., Christenson E. J., and Stein R. A., 1996, "Comparison of Variable Camshaft Timing Strategies at Part Load," SAE Paper No. 960584.

Ma T. H., 1988, "Effects of Variable Engine Valve Timing on Fuel Economy," SAE Paper No. 880390.

Meacham G.-B., 1970, "Variable Cam Timing as an Emission Control Tool," SAE Paper No. 700645.

Moskwa J. J. and Hedrick J. K., 1992, "Modeling and validation of automotive engines for control algorithm development," ASME Journal of Dynamic Systems, Measurement, and Control, Vol. 114, pp. 278-285.

Novak J. M., 1977, "Simulation of the Breathing Process and Air-Fuel Ratio Distribution Characteristics of Three-Valve, Stratified Charge Engines," SAE Paper No. 770881.

Powell B. K. and Cook J. A., 1987, "Nonlinear Low Frequency Phenomenological Engine Modeling and Analysis," Proc. 1987 Amer. Contr. Conf., Vol. 1, pp. 332-340.

Schechter M. M. and Levin M. B., 1996, "Camless Engine," SAE Paper No. 960581.

Stefanopoulou A. G., 1996, "Modeling and Control of Advanced Technology Engines", Ph. D. Dissertation, The University of Michigan, Ann Arbor, MI.

Stein R. A., Galietti K. M., and Leone T. G., 1995, "Dual Equal VCT- A Variable Camshaft Timing Strategy for Improved Fuel Economy and Emissions," SAE Paper No. 950975.

Throop M. J., Cook J. A., and Hamburg D. R., 1985, "The Effect of EGR System Response Time on NO_x feedgas Emissions during Engine Transients," SAE Paper No. 850133.

Appendix

A Regression Maps

The information in this appendix is complementary to Section 4, and provides all the nonlinear regression maps. The regression analysis was based on least squares estimate. In the least squares estimation we used normalized variables to a range from 0 to 1 based on the following conversion:

$$\hat{y} = \frac{y - y_{min}}{y_{max} - y_{min}} \tag{21}$$

where y_{min} and y_{max} is the minimum and maximum output value of the data set used, and

$$\hat{x} = \frac{x - x_{min}}{x_{max} - x_{min}} \tag{22}$$

where x_{min} and x_{max} is the minimum and maximum input value of the data set used.

Sonic Mass Air Flow Rate through the Throttle Body		
$g_2(\theta) = F(\theta)$		
$y = \dot{m}_\theta$, g/sec	$y_{min} = 4.02$	$y_{max} = 52.0558$
$x = \theta$, degrees	$x_{min} = 0.36$	$x_{max} = 19.2$
$\hat{y} = 0.0062 + 0.0537\hat{x} + 1.6134\hat{x}^2 - 0.6994\hat{x}^3$		

Engine Pumping Mass Air Flow Rate		
$\dot{m}_{cyl} = F(CAM, P_m, N)$		
$y = \dot{m}_{cyl}$, g/sec	$y_{min} = 3.67$	$y_{max} = 54.09$
$x =$ CAM, degrees P_m, bar N, RPM	$x_{min} =$ 0 0 0	$x_{max} =$ 35 1 2000
$\hat{y} = -0.1231 - 0.1088\hat{x}_1 + 0.3396\hat{x}_2 - 0.1386\hat{x}_3 + 0.1438\hat{x}_1\hat{x}_3 + 0.0043\hat{x}_3^3$ $+0.1899\hat{x}_1\hat{x}_2 + 1.4548\hat{x}_2\hat{x}_3 + 0.0186\hat{x}_1^2 - 0.8495\hat{x}_2^2 - 0.0080\hat{x}_3^2 - 0.0854\hat{x}_1^2\hat{x}_3$ $-0.0962\hat{x}_1^2\hat{x}_2 - 0.0992\hat{x}_3^2\hat{x}_1 + 0.1855\hat{x}_3^2\hat{x}_2 - 0.1881\hat{x}_2^2\hat{x}_1 - 0.1881\hat{x}_2^2\hat{x}_1$ $-0.4097\hat{x}_2^2\hat{x}_3 - 0.1900\hat{x}_1\hat{x}_2\hat{x}_3 + 0.0121\hat{x}_1^3 + 0.7603\hat{x}_2^3$		

Torque Response		
$T_q = F(m_{cyl}, A/F, N)$		
$y = T_b$, Nm	$y_{min} = -21.71$	$y_{max} = 247.6$
$x =$ m_{cyl}, g/int. ev. A/F N, RPM	$x_{min} =$ 0.0606 11.7 745	$x_{max} =$ 0.4 16.3 2005
$\hat{y} = 0.0480 + 1.2995\hat{x}_1 - 0.0061\hat{x}_2 - 0.0814\hat{x}_3 + 0.0620\hat{x}_1\hat{x}_3 + 0.2514\hat{x}_1\hat{x}_2$ $+0.0218\hat{x}_2\hat{x}_3 - 0.6635\hat{x}_1^2 - 0.0835\hat{x}_2^2 + 0.0544\hat{x}_3^2 + 0.2048\hat{x}_1^2\hat{x}_3 - 0.0779\hat{x}_1^2\hat{x}_2$ $-0.1381\hat{x}_3^2\hat{x}_1 - 0.0179\hat{x}_3^2\hat{x}_2 - 0.2113\hat{x}_2^2\hat{x}_1 + 0.0077\hat{x}_2^2\hat{x}_3 - 0.0308\hat{x}_1\hat{x}_2\hat{x}_3$ $+0.2602\hat{x}_1^3 + 0.0436\hat{x}_2^3 - 0.0153\hat{x}_3^3$		

Feedgas Emission of Oxides of Nitrogen

$$NO_x = F(N, CAM, A/F, P_m)$$

$y = NO_x$, g/kW-h | $y_{min} = 3.67$ | $y_{max} = 54.09$

$$x = \begin{bmatrix} N, \text{ RPM} \\ CAM, \text{ degrees} \\ A/F \\ P_m, \text{ bar} \end{bmatrix} \quad x_{min} = \begin{bmatrix} 746 \\ -0.2 \\ 11.7 \\ 0.148 \end{bmatrix} \quad x_{max} = \begin{bmatrix} 2005 \\ 35.1 \\ 16.43 \\ 0.617 \end{bmatrix}$$

$$\begin{aligned}
\hat{y} \quad &= 0.0200 + 0.0529\hat{x}_1 - 0.0017\hat{x}_1^2 - 0.0266\hat{x}_2 + 0.0667\hat{x}_1\hat{x}_2 - 0.0946\hat{x}_1^2\hat{x}_2 \\
&-0.6872\hat{x}_3\hat{x}_4 + 0.1718\hat{x}_3 + 0.7840\hat{x}_1\hat{x}_3 + 0.1668\hat{x}_1^2\hat{x}_3 - 0.3265\hat{x}_2\hat{x}_3 + 0.0074\hat{x}_1\hat{x}_2\hat{x}_3 \\
&-0.5876\hat{x}_3^2 + 0.0256\hat{x}_1\hat{x}_3^2 - 0.2354\hat{x}_1^2\hat{x}_3^2 + 0.8155\hat{x}_2\hat{x}_3^2 - 1.9732\hat{x}_1\hat{x}_2\hat{x}_3^2 + 1.8512\hat{x}_1^2\hat{x}_2\hat{x}_3^2 \\
&+0.2188\hat{x}_3^3 + 0.5549\hat{x}_1\hat{x}_3^3 - 0.7877\hat{x}_1^2\hat{x}_3^3 - 0.1859\hat{x}_2\hat{x}_3^3 + 0.0721\hat{x}_1\hat{x}_2\hat{x}_3^3 + 0.1120\hat{x}_1^2\hat{x}_2\hat{x}_3^3 \\
&+0.2712\hat{x}_4 + 0.0067\hat{x}_1\hat{x}_4 + 0.0966\hat{x}_1^2\hat{x}_4 - 0.0932\hat{x}_2\hat{x}_4 - 0.7164\hat{x}_1\hat{x}_2\hat{x}_4 + 0.7201\hat{x}_1^2\hat{x}_2\hat{x}_4 \\
&+1.5405\hat{x}_1\hat{x}_2\hat{x}_3\hat{x}_4 - 1.8901\hat{x}_1^2\hat{x}_2\hat{x}_3\hat{x}_4 + 11.2350\hat{x}_3^2\hat{x}_4 - 1.4304\hat{x}_1\hat{x}_3^2\hat{x}_4 + 4.1765\hat{x}_1^2\hat{x}_3^2\hat{x}_4 \\
&+8.1200\hat{x}_1\hat{x}_2\hat{x}_3^2\hat{x}_4 + 2.4157\hat{x}_1^2\hat{x}_2\hat{x}_3^2\hat{x}_4 - 7.8180\hat{x}_3^3\hat{x}_4 + 0.2633\hat{x}_1\hat{x}_3^3\hat{x}_4 - 15.7908\hat{x}_2\hat{x}_3^2\hat{x}_4 \\
&+0.6803\hat{x}_1\hat{x}_2\hat{x}_3^3\hat{x}_4 - 7.1907\hat{x}_1^2\hat{x}_2\hat{x}_3^3\hat{x}_4 - 0.1626\hat{x}_4^2 - 0.1804\hat{x}_1\hat{x}_4^2 - 0.0598\hat{x}_1^2\hat{x}_4^2 \\
&+1.3561\hat{x}_1\hat{x}_2\hat{x}_4^2 - 1.1440\hat{x}_1^2\hat{x}_2\hat{x}_4^2 + 2.6223\hat{x}_2\hat{x}_3\hat{x}_4 - 1.0828\hat{x}_3\hat{x}_4^2 + 5.5225\hat{x}_1\hat{x}_3\hat{x}_4^2 \\
&-2.3212\hat{x}_2\hat{x}_3\hat{x}_4^2 - 3.8016\hat{x}_1\hat{x}_2\hat{x}_3\hat{x}_4^2 + 3.0169\hat{x}_1^2\hat{x}_2\hat{x}_3\hat{x}_4^2 - 4.3774\hat{x}_3^2\hat{x}_4^2 - 3.3992\hat{x}_1\hat{x}_3^2\hat{x}_4^2 \\
&17.7500\hat{x}_2\hat{x}_3^2\hat{x}_4^2 - 4.3862\hat{x}_1\hat{x}_2\hat{x}_3^2\hat{x}_4^2 - 3.9039\hat{x}_1^2\hat{x}_2\hat{x}_3^2\hat{x}_4^2 + 3.1401\hat{x}_3^3\hat{x}_4^2 - 3.4572\hat{x}_1\hat{x}_3\hat{x}_4 \\
&+1.0739\hat{x}_1\hat{x}_3^3\hat{x}_4^2 + 4.6572\hat{x}_1^2\hat{x}_3^3\hat{x}_4^2 - 9.6303\hat{x}_2\hat{x}_3^3\hat{x}_4^2 - 3.2302\hat{x}_1\hat{x}_2\hat{x}_3^3\hat{x}_4^2 + 7.3144\hat{x}_1^2\hat{x}_2\hat{x}_3^3\hat{x}_4^2 \\
&-0.6932\hat{x}_1^2\hat{x}_2\hat{x}_3 + 8.9838\hat{x}_2\hat{x}_3^3\hat{x}_4 - 1.3755\hat{x}_1^2\hat{x}_3^3\hat{x}_4 - 6.3261\hat{x}_1^2\hat{x}_3^2\hat{x}_4^2 + 0.5724\hat{x}_1^2\hat{x}_3\hat{x}_4 \\
&-0.0399\hat{x}_2\hat{x}_4^2 - 0.4514\hat{x}_1^2\hat{x}_3\hat{x}_4^2 \ .
\end{aligned}$$

Feedgas Emissions of Hydrocarbons

$$HC = F(N, CAM, A/F, P_m)$$

$y = HC$, g/kW-h | $y_{min} = 2.59$ | $y_{max} = 97.05$

$$x = \begin{bmatrix} N, \text{ RPM} \\ CAM, \text{ degrees} \\ A/F \\ P_m, \text{ bar} \end{bmatrix} \quad x_{min} = \begin{bmatrix} 746 \\ -0.2 \\ 11.7 \\ 0.148 \end{bmatrix} \quad x_{max} = \begin{bmatrix} 2005 \\ 35.1 \\ 16.43 \\ 0.617 \end{bmatrix}$$

$$\begin{aligned}
\hat{y} \quad &= 0.0230 + 0.0350\hat{x}_3 - 0.0662\hat{x}_3^2 + (0.5933 - 1.1822\hat{x}_3 + 1.3418\hat{x}_3^2)\hat{x}_1 \\
&+(-1.4062 + 3.0186\hat{x}_3 - 3.6013\hat{x}_3^2)\hat{x}_1^2 + (0.9045 - 2.1751\hat{x}_3 + 2.6315\hat{x}_3^2)\hat{x}_1^3 \\
&[+0.0171 - 0.0347\hat{x}_3 + 0.0405\hat{x}_3^2 + (-0.1416 + 0.3203\hat{x}_3 - 0.3480\hat{x}_3^2)\hat{x}_1 \\
&+(0.3138 - 0.7474\hat{x}_3 + 0.7988\hat{x}_3^2)\hat{x}_1^2 + (-0.1891 + 0.4611\hat{x}_3 - 0.4906\hat{x}_3^2)\hat{x}_1^3]\frac{1}{\hat{x}_4} \\
&-0.6905\hat{x}_2 + 0.6338\frac{\hat{x}_2}{\hat{x}_4^{1/16}}
\end{aligned}$$